

# Experimental evidence of disorder enhanced electron-phonon scattering in graphene devices

Charalambos Evangelis,<sup>\*,†,§</sup> Edward McCann,<sup>‡,§</sup> Jacob L. Swett,<sup>†</sup> Sumit Tewari,<sup>†</sup>  
Xinya Bian,<sup>†</sup> James Thomas,<sup>†</sup> G. Andrew D. Briggs,<sup>†</sup> Oleg V. Kolosov,<sup>\*,‡</sup> and  
Jan A. Mol<sup>¶</sup>

<sup>†</sup>*Department of Materials, University of Oxford, Parks Road, OX1 3PH, Oxford, United Kingdom*

<sup>‡</sup>*Department of Physics, Lancaster University, Bailrigg, LA1 4YB, Lancaster, United Kingdom*

<sup>¶</sup>*School of Physics and Astronomy, Queen Mary University of London, London E1 4NS, United Kingdom*

<sup>§</sup>*Equal contribution*

E-mail: charalambos.evangelis@materials.ox.ac.uk; o.kolosov@lancaster.ac.uk

## Abstract

Induced disorder in graphene enables changes in the electrical and thermal transport. It has been shown previously that disorder is very important for electron cooling in graphene through disorder-assisted electron-phonon scattering, particularly via the supercollisions process. Here we study electron momentum relaxation due to electron-phonon scattering while increasing the degree of disorder. With in-situ Scanning Thermal Microscopy we monitor the temperature rise in the constriction of a bowtie-shaped graphene device while increasing the disorder by means of feedback-controlled voltage ramps at high-currents. Analysis of the combined thermal and electrical measurements

shows that, the relative change of the momentum scattering rate vs temperature, as measured at room temperature, increases with strong local disorder. By excluding candidate mechanisms for this phenomenon, including a change of the charge density and activation of optical phonons, we conclude that the observed increase in the temperature dependent part of the scattering rate is likely due to new acoustic phonon scattering channels that open up as disorder increases.

## Introduction

Understanding momentum relaxation mechanisms of electrons with different degrees of disorder, especially at room temperature, is of prime importance for many electronic applications of graphene and other van-der-Waals (vdW) conductive materials. For example, the use of graphene as an interconnect in electronic circuits necessitates high electrical currents while requiring efficient heat dissipation to avoid breakdown.<sup>1</sup> Under high-current density, graphene is Joule-heated to extremely high temperatures. Electron mobility becomes limited due to electron scattering by phonons and disorder including impurities, defects and vacancies,<sup>2</sup> and, as a result, the current saturates and the temperature rises. High temperature results in oxidation of graphene in air, or sublimation in vacuum, and, finally, breakdown of graphene.<sup>3,4</sup> In some cases, high temperature could also be catastrophic for the substrates, due to their lower melting point compare to graphene especially in vacuum environments.

In graphene the main mechanisms of electron energy relaxation are scattering with acoustic phonons, impurities and phonons (supercollisions), and optical phonons for very low, intermediate and extremely high temperatures, respectively.<sup>5,6</sup> Energy relaxation is found to increase with disorder produced by thermal treatment<sup>7</sup> or by optically added defects.<sup>8</sup>

In this work, we study momentum relaxation mechanisms of electrons during transport in graphene nanoscale bowtie shape devices at room temperature and high vacuum. We increase the degree of disorder in a controlled manner, by feedback-controlled voltage ramps at high-current close to breakdown limits while monitoring the temperature with a Scanning

Thermal Microscope (SThM). We then develop an analytical model, fit the data and show that the electron-phonon momentum scattering rate increases with increased disorder at room temperature. After considering different possible origins of this observation including change in the charge density and optical phonons activation, we conclude that new acoustic phonon channels are enabled possibly due to strong disorder-assisted phonon scattering.

# Results and discussion

## Feedback controlled breakdown

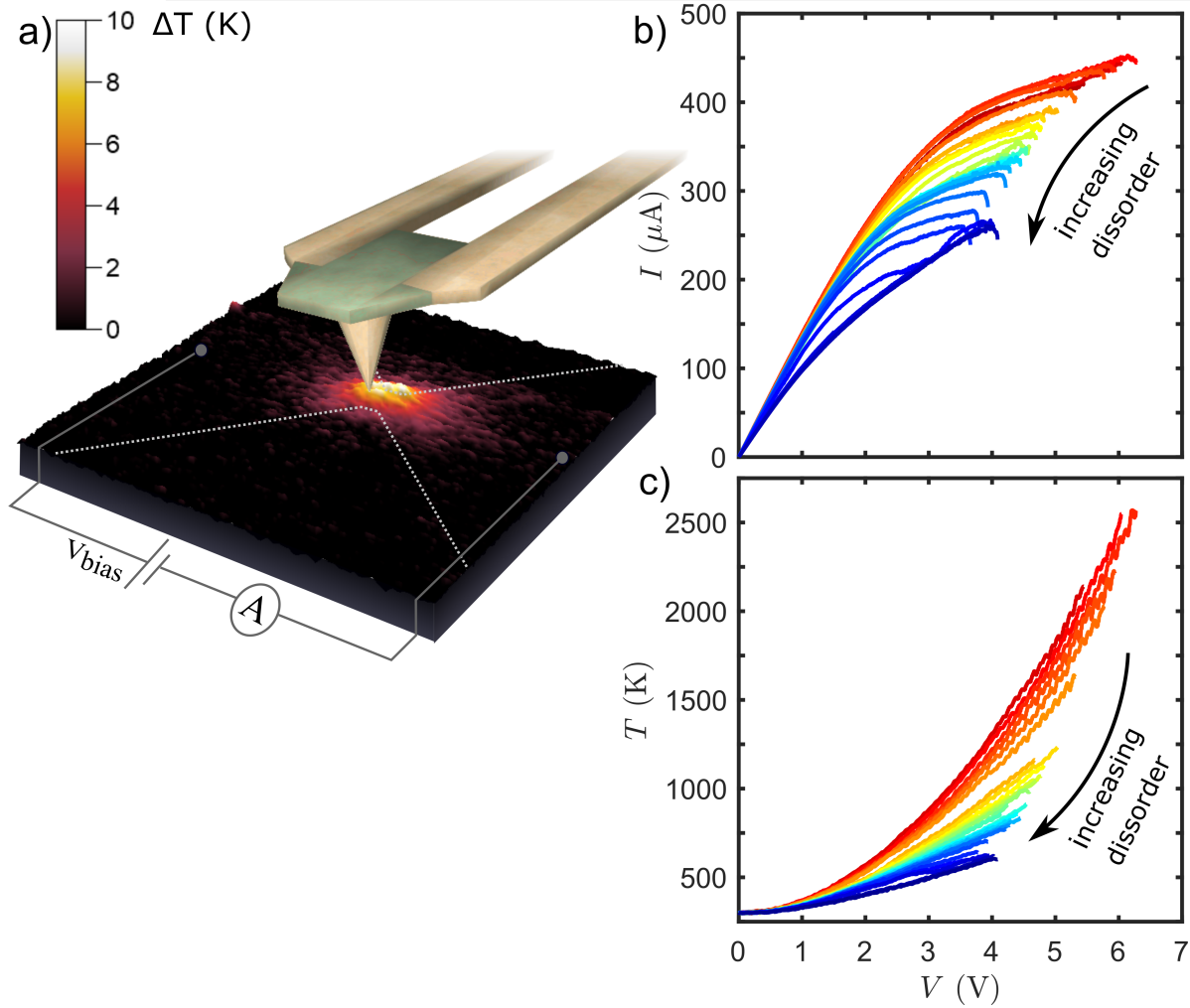


Figure 1: (a) Schematic representation of the High Vacuum measurement, with a typical temperature map of the graphene nanoconstriction (scan dimensions  $2.5 \times 2.5 \mu m$ ). Color bar indicates the excess temperature with respect to room temperature ( $\Delta T = T - T_0$ ) (b,c) Current vs Voltage curves of the initial cycles of feedback controlled breakdown of graphene devices (b) and the corresponding temperature during the process (c).

To simultaneously study the electrical and thermal properties of a graphene bowtie nanoconstriction (see Methods for fabrication details), we have developed a specialized high-vacuum chamber equipped with a scanning thermal microscope (SThM) for thermal imaging<sup>9,10</sup> and

feed-throughs for electrical characterization. The SThM operates like a conventional atomic force microscope, except that a high electrical resistance area at the end of the cantilever close to the probe tip, acts as a heater or thermometer. By applying a voltage to the resistive area, the probe is heated and when the tip is in contact with the sample, the temperature of the probe and thus the resistance of the heater changes depending on the heat transfer between the tip and the sample.<sup>11</sup> The resistance variations are transformed into temperature through the probe calibration and modeling of the tip-sample thermal circuit (see methods and SI note 1).

During our measurements, we first apply a small bias voltage across the devices ( $V_b = 0.5\text{V}$ ) to spatially map the temperature.<sup>12</sup> Figure 1a shows a typical temperature map: the temperature is highest near the narrow part of the graphene constriction due to the higher current density and resulting Joule heating in this region.<sup>13</sup> The temperature increase is localized to the graphene and  $\text{SiO}_2$  area near the constriction as a result of the poor thermal conductivity of  $\text{SiO}_2$  and the  $\text{SiO}_2$ /graphene interface, which makes the nanoconstriction an inefficient heat spreader despite the high thermal conductivity of the graphene.<sup>9</sup>

Next, we investigate the electrical and thermal properties of the graphene nanoconstriction when a large bias voltage, close to the breakdown limit, is applied across it. To do so, we place the SThM tip at the center of the constriction where the highest temperature was detected. We simultaneously monitor the current and temperature whilst we increase the voltage across the nanoconstriction as shown in Figure 1b. To prevent uncontrolled electrical breakdown of the graphene, we employ a feedback method that has previously been used to fabricate graphene tunnel junctions for single-molecule studies.<sup>14</sup> This method allows us to controllably Joule heat the graphene to the maximum limit, where the breakdown initiates and gradually increase the amount of disorder in the nanoconstriction via a cyclical process. During each cycle the voltage across the constriction is slowly ( $5 - 8\text{Vs}^{-1}$ ) ramped up from zero. When the current through the constriction begins to drop, due to the onset of breakdown of the graphene, the voltage is quickly ( $2500 - 5000\text{Vs}^{-1}$ ) ramped back down

to zero.

By comparing the current and temperature traces as a function of bias voltage, we observe that: i) the differential conductance  $dI/dV_b$  decreases with increasing temperature in each cycle; and ii) the maximum current and temperature that are reached before the onset of breakdown decrease from one cycle to the next. We note here that even if the qualitative trend of the temperature with the number of cycles is robust for each device, comparison between the temperature maps or traces for different devices is non-trivial due to the SThM tip and contact thermal resistance influence on the measurement (see SI note 1). In the next sections we will show how these observations reveal of an increase in the electron-phonon scattering rate with increasing disorder in the graphene nanoconstriction.

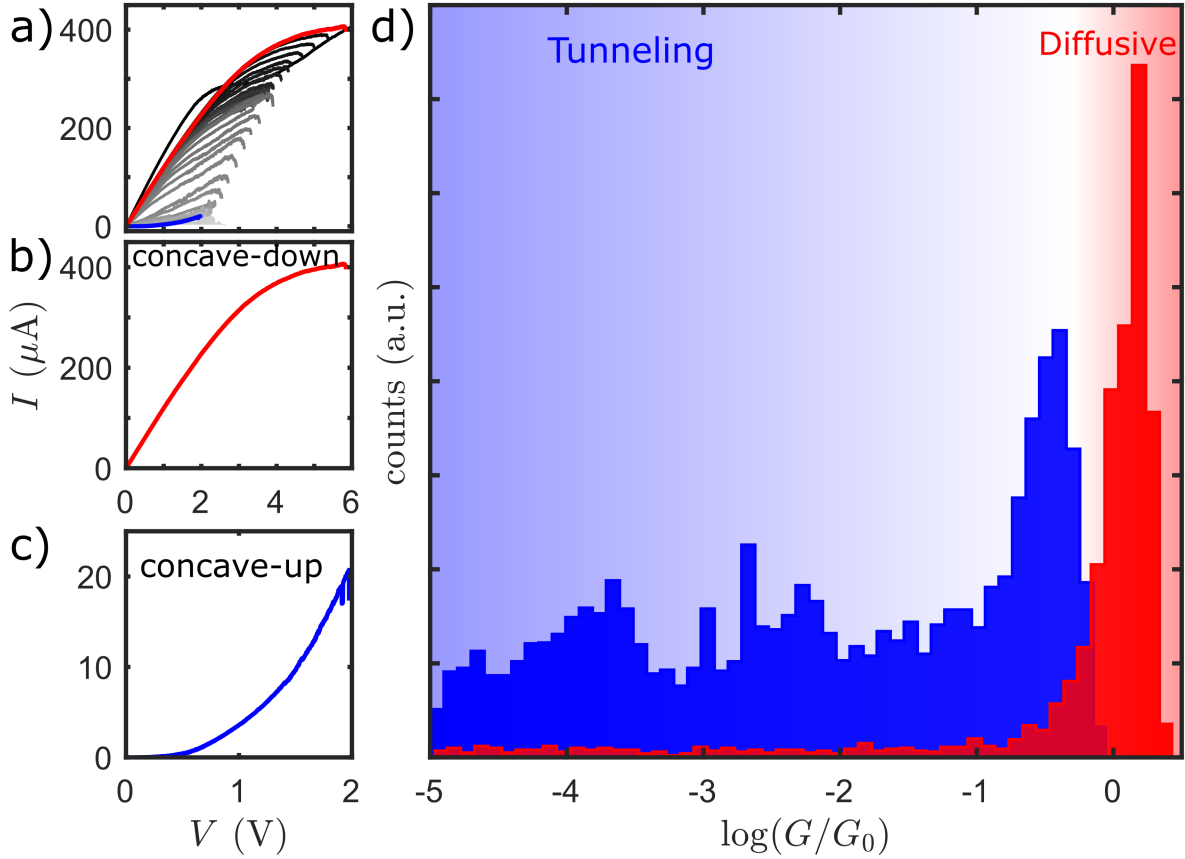


Figure 2: (a) Typical example of  $I - V$  curves during the feedback-controlled breakdown process. (b,c) Examples of I-V curves showing: high-field diffusive (b) and tunneling (c) transport. (d) Histogram of zero-bias conductance ( $\log(G/G_0)$ ) for cycles with tunneling behaviour (blue) and high-field diffusive transport (red) for 138 devices.

When we investigate the current-voltage ( $I - V$ ) curves for individual cycles, we observe that these can be either concave downward ( $d^2I/dV^2 < 0$ ) or concave upward ( $d^2I/dV^2 > 0$ ). This separation is further evidenced by a statistical analysis of the zero-bias conductance of a total of 10634 cycles measured over 138 devices, as shown in Figure 2. We find that, the large majority of concave downward curves have a zero-bias conductance greater than the conductance quantum  $G_0 = 2e^2/h = 7.7 \times 10^{-5}$  S, and which we therefore attribute to diffusive transport while the concave upward curves have a zero-bias conductance less than  $G_0$  and we therefore attribute to transport across single or multiple potential barriers. The transition from diffusive transport to transport across one or more potential barriers is a

direct result of the gradually increasing disorder in the graphene nanoconstriction. At the end of each cycle, Joule heating leads to an increase in the number of scattering sites which eventually form potential barriers in the graphene nanoconstriction. While the atomistic details of this process are not known, studies of electric breakdown of graphene under different atmospheres have suggested that - depending on the oxygen concentration of the sample surroundings - Joule heating either leads to oxidation or sublimation of the graphene,<sup>15-17</sup> thereby increasing the amount of disorder.

The concave upwards curves at room temperature for  $G < G_0$  are consistent with our previous observation of the gradual transition from multi-mode Fabry-Pérot interference to sequential electron tunneling (Coulomb blockade) across one or more graphene islands to the formation of tunnel junctions with decreasing conductance below  $G_0$  at cryogenic temperatures.<sup>18</sup> The appearance of peaks in the conductance histogram could point to the preferential formation of specific atomic configurations, such as carbon chains,<sup>19-21</sup> or be related to transport through the SiO<sub>2</sub>/graphene interface.<sup>22</sup> Unravelling the details of tunneling transport of graphene constriction of unknown characteristics can be complicated and it is beyond the scope of this study and therefore in the following we focus on electronic and thermal transport in the diffusive transport regime.

## Analytical model of Joule heating and electronic transport

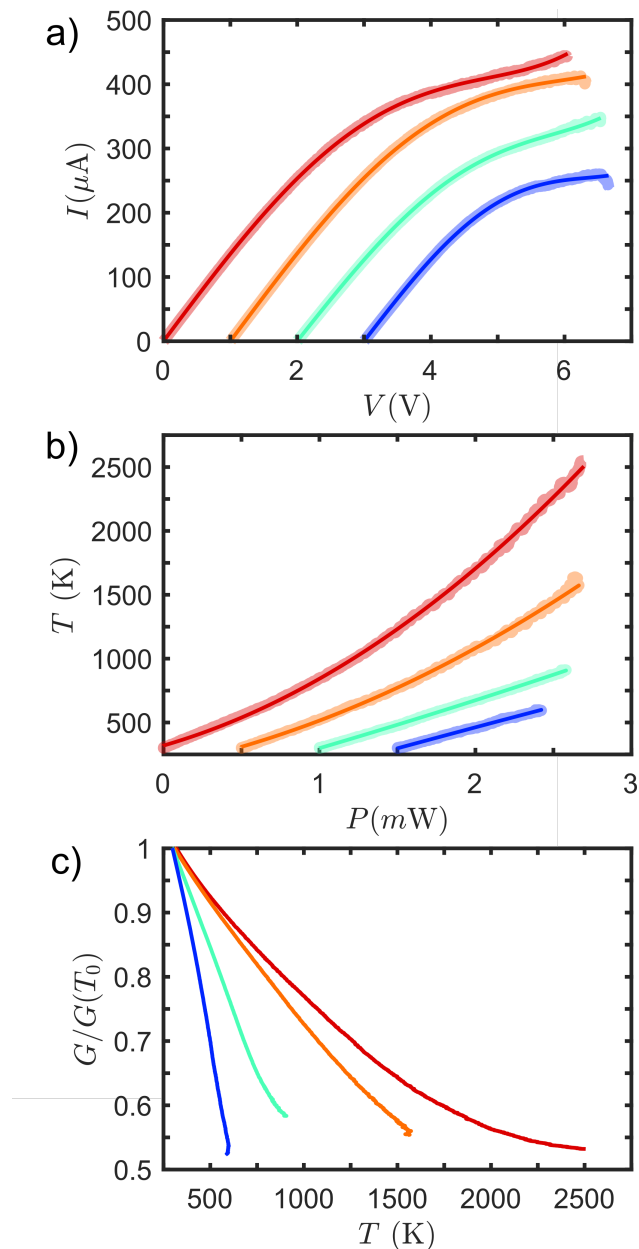


Figure 3: (a,b,c) Examples of: measured (thick transparent line) and fitted from the model (solid line)  $I - V$  curves (a), Temperature versus Power (as calculated arithmetically from each  $I - V$  curves) (b) and Conductance as calculated from the fitted to the model curves with Temperature (c). Note that the examples are curves taken from the device presented in Figure 1 of the 2<sup>nd</sup>, 6<sup>th</sup>, 15<sup>th</sup> and 23<sup>rd</sup> cycle. For the fittings we used Equation 1 and 2 with up to 3rd order terms included.

In the diffusive transport regime, the current initially increases linearly with voltage and gradually saturates at higher voltages. The maximum current density in the constriction as calculated out of the first  $I - V$  cycle is  $9.1 \times 10^8 \text{Acm}^{-2}$  which is in the same order as previously reported for graphene devices.<sup>23</sup> We develop an analytical model which shows that our experiments are able to extract the logarithmic derivative of the momentum scattering rate with respect to temperature. The non-Ohmic behavior at higher voltages (see Figure 1a) and the exponential increase of the temperature (see Figure 1b) suggests phonon-assisted transport at high-fields. The scattering rate in high voltage regime is 6 times larger than in the low voltage regime for the first  $I - V$  cycle as calculated from the conductance ratio at the two regimes. More specifically, we assumed that the temperature dependent conductance  $G(T)$  depends linearly on the momentum scattering time  $\tau(T)$  and thus its ratio at the two different regimes is equivalent to the scattering rate ratio. We then expand  $G(T)$  around room temperature,  $T_0$ , as

$$G(T) = G(T_0) \left( 1 - \Delta T \frac{d \ln \tau^{-1}}{dT} \Big|_{T=T_0} + \dots \right), \quad (1)$$

where the temperature rise  $\Delta T = T - T_0$  due to Joule heating is related to the power  $P$  injected. By expanding  $T(P)$  at  $T_0$ , with  $T_0 = T(0)$ , the temperature rise in the device may be written as

$$\Delta T = P \frac{dT}{dP} \Big|_{T=T_0} + \dots, \quad (2)$$

and by substituting Equation 1 and 2 in  $I = GV$  with  $P = IV$ , we obtain for the current valid up to cubic order in  $V$ ,

$$I = G(T_0)V - \gamma G^2(T_0)V^3 + \dots, \quad (3)$$

where  $\gamma = \frac{dT}{dP} \frac{d \ln \tau^{-1}}{dT} \Big|_{T=T_0}$ . Hence, the logarithmic derivative of the momentum scattering rate with respect to temperature, i.e. the relative change of the scattering rate at room

temperature, is given by

$$\left. \frac{d}{dT} \ln \tau^{-1} \right|_{T=T_0} = \frac{\gamma}{dT/dP|_{T=T_0}}. \quad (4)$$

It is possible to determine the relative change of the scattering rate from the experimental data because  $dT/dP|_{T=T_0}$  and  $\gamma$  are fitting parameters of Equation 2 and 3 to the  $P - T$  and  $I - V$  characteristics of each cycle, respectively (see Figure 3 a and b for representative examples).

From Equation 1 it can be shown that the relative change of the scattering rate at  $T_0$  is the derivative of the normalized (by zero-bias conductance) conductance at room temperature,  $G/G(T_0)$ . Figure 3c shows examples of  $G/G(T_0)$  traces with temperature as calculated from the fitted  $I - V$  traces, with temperature for different cycles and therefore degree of disorder. Unexpectedly, we find that the derivative of  $G/G(T_0)$  at  $T_0$ , and thus the relative change of the momentum scattering rate at  $T_0$ , increases with disorder. One would expect the opposite, since  $\tau^{-1}$  itself increases with increasing disorder.

To understand this counterintuitive result we take into account disorder and phonons as sources of momentum relaxation. We assume a temperature-independent scattering rate  $\tau_d^{-1}$  due to static disorder such as charged Coulomb impurities or vacancies and a number of temperature-dependent electron-phonon rates  $\tau_i^{-1}(T)$ , where  $i$  indexes different phonon modes, so that  $\tau^{-1} = \tau_d^{-1} + \sum_i \tau_i^{-1}(T)$  and

$$\left. \frac{d}{dT} \ln \tau^{-1} \right|_{T=T_0} = \frac{\sum_i \Delta_i(T_0)}{\tau_d^{-1} + \sum_i \tau_i^{-1}(T_0)}, \quad (5)$$

where  $\Delta_i(T_0) = \left. \frac{d}{dT} (\tau_i^{-1}(T)) \right|_{T=T_0}$ . In other words, the relative change of the scattering rate at  $T_0$  is given by the change of the scattering rates due to phonons divided by the total scattering rate, all evaluated at temperature  $T_0$ .

Assuming that scattering rates due to acoustic phonons exhibit a generic power law dependence on temperature  $\tau_\alpha^{-1}(T) \sim T^\alpha$ , then  $\Delta_\alpha(T_0) \sim \alpha T_0^{\alpha-1}$  (theory predicts that  $\alpha = 1$  for graphene near room temperature).<sup>24,25</sup> At room temperature and near the chemical

potential, the rate due to optical phonons with frequency  $\omega_0$  will be exponentially suppressed  $\tau_o^{-1}(T) \sim \exp(-\hbar\omega/k_B T_0)$  yielding  $\Delta_i(T_0) \sim \hbar\omega/k_B T_0^2 \exp(-\hbar\omega/k_B T_0)$  (see SI note 6). Given that  $\omega_0 \approx 200\text{meV}$  in graphene,<sup>26–28</sup> this contribution is very small in room temperature  $T_0$ , and we neglect it in the following.

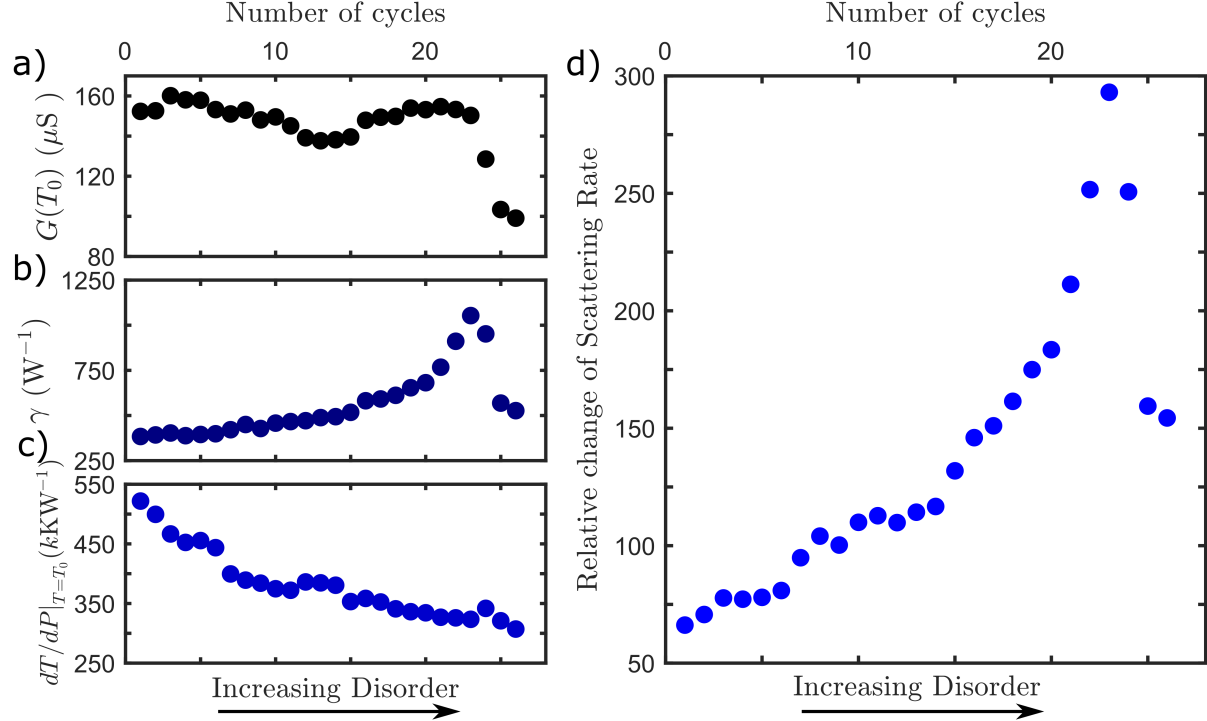


Figure 4: (a,b,c,d) Conductance at room temperature  $G(T_0)$  (a), parameter  $\gamma$  (b),  $dT/dP|_{T=T_0}$  (c) and relative change of Scattering rate (d) with the number of cycles (i.e. increasing disorder) for the device presented in Figure 1.  $G(T_0)$ ,  $\gamma$  and  $dT/dP|_{T=T_0}$  are extracted by fitting Equation 6 and 2 to the I-V and P-T curves presented in Figure 1 and then are used for the calculation of the relative change of  $\tau^{-1}$  with Equation 4

To fit our data, we express the current as

$$I = \frac{1}{2\gamma V} (\sqrt{1 + 4\gamma G(T_0)V^2} - 1), \quad (6)$$

which agrees with Equation 3 up to cubic order in  $V$ . Equation 6 (see SI note 5 for derivation) provides a better fit than truncating the expression at cubic order in  $V$ ; Equation 6 predicts  $I \rightarrow \text{const}$  as  $V \rightarrow \infty$  whereas truncating at cubic order as in Equation 3 gives a wholly

unphysical result  $I \rightarrow -\infty$  as  $V \rightarrow \infty$ . We use Equation 6 to fit the  $I - V$  characteristics of each cycle and obtain  $G(T_0)$  and  $\gamma$  (see Figure 4 a and b, respectively).  $G(T_0)$  shows a general decreasing behavior with the number of cycles with individual values being very close to the zero-bias conductance as measured after each cycle (see SI note 2).  $\gamma$  on the other hand increases up to a point and then starts to decrease at a high degree of disorder. To calculate the normalized electron-phonon scattering rate with disorder we further fit  $P - T$  curves with Equation 2 and obtain  $dT/dP|_{T=T_0}$  (see Figure 4c). The relative change of  $\tau^{-1}$  is found to increase with disorder, however for high degree of disorder it drops sharply (see Figure 4d). This drop is related with the sharp resistance decrease (see Figure 4a) and possibly indicates a transition to different transport regime (i.e. tunneling), not described by our model. Similar trends are obtained for a second device (see SI note 3).

Before focusing on disorder, we briefly discuss the dependence of  $\tau^{-1}$  on charge density which may also change with cycle number. The disorder rate  $\tau_d^{-1}$  originating from charge impurities or vacancies is predicted to decrease with charge density<sup>25</sup> while the acoustic phonon rate should increase with density.<sup>24,25</sup> Thus, an increase of charge density with cycle number would explain the observed behavior of  $\tau^{-1}$ . To check this hypothesis, we swept the back-gate voltage of our devices while recording the current after each voltage ramp cycle (see SI note 2). We found that the Dirac point minimum becomes less defined after each cycle which is consistent with an increase in disorder, but it shifts from positive gate voltages towards zero with increasing number of cycles. This would indicate a decrease of charge density which is the opposite trend to what is needed to explain the observed behavior of the scattering rate.

The scattering rate due to disorder  $\tau_d^{-1} = v_F/l$ , where  $v_F$  is the Fermi velocity and  $l$  is the electron mean free path, increases with the degree of disorder. For the relative change of  $\tau^{-1}$  to increase with disorder, as is observed, the scattering rate due to phonons ( $\tau_p^{-1}$ ) must increase with disorder faster than  $\tau^{-1}$  itself (where  $\tau^{-1} \geq \tau_d^{-1}$ ). We attribute this behavior to new phonon scattering channels that open up as disorder increases. Theoretical modeling

of electron momentum relaxation due to acoustic phonons in graphene has focused on the ballistic limit<sup>24,25</sup> whereby

$$\tau_{\text{ballistic}}^{-1}(T) = \frac{2\pi}{\hbar} \lambda k_{\text{B}} T. \quad (7)$$

where  $\lambda$  is the dimensionless electron-phonon coupling constant. Disorder-assisted phonon scattering events, known as supercollisions, have been discussed at length in the context of electron cooling.<sup>6,7,29</sup> Using a perturbative calculation for weak disorder  $k_{\text{F}} l \gg 1$ , where  $k_{\text{F}}$  is the Fermi wavevector, Song et al<sup>29</sup> considered the influence of supercollisions on momentum relaxation,

$$\tau_{\text{super}}^{-1}(T) = \frac{4\pi}{\hbar k_{\text{F}} l} \lambda k T \ln(T/T_{\text{BG}}), \quad (8)$$

where  $T_{\text{BG}}$  is the Bloch Grüneisen temperature and  $T_0 \gg T_{\text{BG}}$  for room temperature  $T_0$ . The supercollision rate  $\tau_{\text{super}}^{-1}(T)$  increases with the degree of disorder (as  $k_{\text{F}} l$  decreases). If it were the only acoustic rate,  $\tau_{\text{ballistic}}^{-1}(T)$  would ensure the relative change of  $\tau^{-1}$  decreases with disorder, the opposite trend to that observed, whereas the addition of  $\tau_{\text{super}}^{-1}(T)$  would lead to a saturation of the relative change of  $\tau^{-1}$ . We stress that the supercollision rate  $\tau_{\text{super}}^{-1}(T)$  is only first order in the perturbative parameter  $1/k_{\text{F}} l$  and we speculate that there are yet more channels for electron-phonon scattering that become relevant as the degree of disorder increases and that dominate in the limit of strong disorder  $k_{\text{F}} l \sim 1$ . Indeed, in the context of thermal transport, numerical modelling has shown that vacancies induce localization of acoustic phonons which leads to a drastic reduction in thermal conductivity.<sup>30,31</sup> An indication of what could happen with electron-phonon scattering is given by examining the form of the electron-phonon coupling constant in the deformation potential approximation,  $\lambda \sim v_{\alpha}^{-2}$  where  $v_{\alpha}$  is the phonon velocity. This suggests phonon localization due to vacancies should dramatically enhance  $\lambda$  and the electron-phonon scattering rate; such an increase could account for the increase with disorder of the relative change of  $\tau^{-1}$  observed in our

experiments.

Although our study of momentum relaxation only required us to consider Joule heating in a general way, as in Equation 2, it is possible to extract further information about heat transport from our data. As described in detail in the SI (see SI note 5), we assume that the thermal conductivity is independent of temperature and that the heat is dissipated into the substrate, rather than, say, via electron thermalization in the leads. Then, under the condition that the thermal healing length ( $L_H = \sqrt{\kappa R_B}$ )<sup>32</sup> is much shorter than the system size, the slope of the  $T(P)$  curve,  $dT/dP|_{T=T_0}$ , is equivalent to the thermal resistance  $R_B$  of the graphene/SiO<sub>2</sub> interface per unit area  $R_B/A$  ( $A$  is the surface area of graphene). Hence, Figure 4c shows that  $R_B/A$  decreases with the number of cycles meaning that more power can be dissipated into the substrate for a certain temperature as the disorder increases. This might be a result of some changes in the graphene effective size and/or the interface with SiO<sub>2</sub>. More specifically, a decrease of the effective size of the device is possible due to sublimation of graphene; naively, a reduction of  $A$  should increase the ratio  $R_B/A$  but, at the same time, reduced size can actually improve dissipation via 3D heat spreading into the substrate.<sup>3</sup> The high local temperatures might also account for some changes in the graphene/SiO<sub>2</sub> interface due to the high local temperatures (eg. sublimation of trapped adsorbates) which result in better heat dissipation to the substrate.

## Outline

In summary, we were able to study the momentum relaxation mechanisms of electrons with increased disorder by measuring the temperature of a graphene device while ramping the bias voltage up to the breakdown limit. By feedback-controlled voltage ramps the graphene is Joule heated and the amount of disorder is controllably increased. We developed a model for calculating the relative change of the momentum scattering rate with temperature from the current-voltage and power-temperature characteristics acquired during the process. By applying the model we show that the relative change of the momentum scattering rate

increases with disorder at room temperature as a result of the increased electron-phonon scattering rate. We attribute this, to new acoustic phonon scattering channels that open up as disorder increases possibly due to disorder-assisted phonon scattering. However, for highly disordered graphene, the scattering rate due to disorder increases at a higher rate, possibly indicating a transition to a different transport regime. Finally, we find that the interface thermal resistance decreases with disorder and we associate that to a decrease of the graphene effective size due to sublimation and changes in graphene/SiO<sub>2</sub> interface due to the high temperature. Our correlated conductance and temperature measurements highlight the importance of electronic momentum relaxation due to phonon scattering that limit carrier mobility in disordered graphene nanostructures. In addition to revealing elusive electron-phonon physics in electronic transport, our work has direct implications for the performance of graphene interconnects for next generation CMOS.<sup>33</sup>

## **Experimental**

### **Device Fabrication**

The graphene nanoconstrictions are grown via chemical vapor deposition (Graphenea) and transferred onto a pre-patterned doped Si with 300nm of SiO<sub>2</sub> substrate with Cr/Au electrodes. The graphene is patterned into a 200nm wide bowtie-shaped constriction using electron-beam lithography and oxygen plasma etching.<sup>16</sup>

### **Scanning Thermal Microscopy**

SThM operates like a conventional atomic force microscope, except that a resistive implant on the cantilever close to the tip acts as a heater and thermometer at the same time that is sensitive to the local temperature and thermal resistance variations of the tip-sample contact. The probe forms one leg of a balanced Wheatstone bridge operating at 91 kHz, with the bridge output amplified via a low noise instrumental amplifier, producing the raw

SThM signal. We apply an AC and voltage to the probe and is heated to a temperature of few K higher than the microscope temperature which is monitored with a surface mount Pt resistor. When the tip is in contact with the sample the, resistance of the probe changes depending on the temperature and thermal resistance of the sample. Out of the SThM signal we can map<sup>12</sup> or get the local variation (see SI note 1) of temperature. The SThM signal is converted in temperature through probe electrical resistance versus temperature calibration<sup>34</sup> performed in the high vacuum chamber.

## Acknowledgement

C.E., S.T., X.B., J.T., J.A.M and G.A.D.B. acknowledge the QuEEN Programme Grant (EP/N017188/1). C.E.and G.A.D.B.acknowledge the John Templeton Foundation. O.V.K. acknowledges the GrapheneCore3 grant number 881603 (Graphene Flagship), EU project QUANTIHEAT (Grant 604668), EPSRC project EP/K023373/1, UKRI project NEXGENNA and Paul Instrument Fund, c/o The Royal Society. J.A.M. was supported through the UKRI Future Leaders Fellowship, Grant No. MR/S032541/1, with in-kind support from the Royal Academy of Engineering.

## Author Contributions

C.E. and E.M. contributed equally to this work. J.S., X.B. and J.T. fabricated the devices. C.E., E.M. and J.A.M. drafted the manuscript. C.E., J.S. and O.V.K performed the SThM measurements and interpretation of SThM data. C.E. and J.T performed the transport measurements. C.E. analyzed and processed the data with the help of S.T.. E.M. carried out the theoretical modeling. C.E., O.K. and J.A.M. designed the experiments. All authors contributed to manuscript revision and discussion of the results.

## Supporting Information Available

This will usually read something like: “Experimental procedures and characterization data for all new compounds. The class will automatically add a sentence pointing to the information on-line:

## References

- (1) Barreiro, A.; Lazzeri, M.; Moser, J.; Mauri, F.; Bachtold, A. Transport properties of graphene in the high-current limit. *Physical review letters* **2009**, *103*, 076601.
- (2) Berciaud, S.; Han, M. Y.; Mak, K. F.; Brus, L. E.; Kim, P.; Heinz, T. F. Electron and optical phonon temperatures in electrically biased graphene. *Physical review letters* **2010**, *104*, 227401.
- (3) Liao, A. D.; Wu, J. Z.; Wang, X.; Tahy, K.; Jena, D.; Dai, H.; Pop, E. Thermally limited current carrying ability of graphene nanoribbons. *Physical review letters* **2011**, *106*, 256801.
- (4) Islam, S.; Li, Z.; Dorgan, V. E.; Bae, M.-H.; Pop, E. Role of Joule heating on current saturation and transient behavior of graphene transistors. *IEEE Electron Device Letters* **2013**, *34*, 166–168.
- (5) Ma, Q.; Gabor, N. M.; Andersen, T. I.; Nair, N. L.; Watanabe, K.; Taniguchi, T.; Jarillo-Herrero, P. Competing channels for hot-electron cooling in graphene. *Physical review letters* **2014**, *112*, 247401.
- (6) Graham, M. W.; Shi, S.-F.; Ralph, D. C.; Park, J.; McEuen, P. L. Photocurrent measurements of supercollision cooling in graphene. *Nature Physics* **2013**, *9*, 103.
- (7) Betz, A.; Jhang, S. H.; Pallecchi, E.; Ferreira, R.; Fève, G.; Berroir, J.-M.; Plaçais, B. Supercollision cooling in undoped graphene. *Nature Physics* **2013**, *9*, 109.

- (8) Alencar, T. V.; Silva, M. G.; Malard, L. M.; de Paula, A. M. Defect-induced supercollision cooling of photoexcited carriers in graphene. *Nano letters* **2014**, *14*, 5621–5624.
- (9) Evangeli, C.; Spiece, J.; Sangtarash, S.; Molina-Mendoza, A. J.; Mucientes, M.; Mueller, T.; Lambert, C.; Sadeghi, H.; Kolosov, O. Nanoscale Thermal Transport in 2D Nanostructures from Cryogenic to Room Temperature. *Advanced Electronic Materials* **2019**,
- (10) Pumarol, M. E.; Rosamond, M. C.; Tovee, P.; Petty, M. C.; Zeze, D. A.; Falko, V.; Kolosov, O. V. Direct nanoscale imaging of ballistic and diffusive thermal transport in graphene nanostructures. *Nano Letters* **2012**, *12*, 2906–2911.
- (11) Spiece, J.; Evangeli, C.; Lulla, K.; Robson, A.; Robinson, B.; Kolosov, O. Improving accuracy of nanothermal measurements via spatially distributed scanning thermal microscope probes. *Journal of Applied Physics* **2018**, *124*, 015101.
- (12) Menges, F.; Riel, H.; Stemmer, A.; Gotsmann, B. Quantitative Thermometry of Nanoscale Hot Spots. *Nano Letters* **2012**, *12*, 596–601, PMID: 22214277.
- (13) Harzheim, A.; Spiece, J.; Evangeli, C.; McCann, E.; Falko, V.; Sheng, Y.; Warner, J. H.; Briggs, G. A. D.; Mol, J. A.; Gehring, P.; Kolosov, O. V. Geometrically Enhanced Thermoelectric Effects in Graphene Nanoconstrictions. *Nano Letters* **2018**, *18*, 7719–7725, PMID: 30418781.
- (14) Gehring, P.; Harzheim, A.; Spiece, J.; Sheng, Y.; Rogers, G.; Evangeli, C.; Mishra, A.; Robinson, B. J.; Porfyraakis, K.; Warner, J. H., et al. Field-effect control of graphene–fullerene thermoelectric nanodevices. *Nano Letters* **2017**, *17*, 7055–7061.
- (15) Prins, F.; Barreiro, A.; Ruitenbergh, J. W.; Seldenthuis, J. S.; Aliaga-Alcalde, N.; Vandersypen, L. M. K.; van der Zant, H. S. J. Room-Temperature Gating of Molecular Junctions Using Few-Layer Graphene Nanogap Electrodes. *Nano Letters* **2011**, *11*, 4607–4611, PMID: 22011188.

- (16) Lau, C. S.; Mol, J. A.; Warner, J. H.; Briggs, G. A. D. Nanoscale control of graphene electrodes. *Phys. Chem. Chem. Phys.* **2014**, *16*, 20398–20401.
- (17) El Abbassi, M.; Pósa, L.; Makk, P.; Nef, C.; Thodkar, K.; Halbritter, A.; Calame, M. From electroburning to sublimation: substrate and environmental effects in the electrical breakdown process of monolayer graphene. *Nanoscale* **2017**, *9*, 17312–17317.
- (18) Gehring, P.; Sadeghi, H.; Sangtarash, S.; Lau, C. S.; Liu, J.; Ardavan, A.; Warner, J. H.; Lambert, C. J.; Briggs, G. A. D.; Mol, J. A. Quantum Interference in Graphene Nanoconstrictions. *Nano Letters* **2016**, *16*, 4210–4216.
- (19) Sadeghi, H.; Mol, J. A.; Lau, C. S.; Briggs, G. A. D.; Warner, J.; Lambert, C. J. Conductance enlargement in picoscale electroburnt graphene nanojunctions. *Proceedings of the National Academy of Sciences* **2015**, *112*, 2658–2663.
- (20) Sarwat, S. G.; Gehring, P.; Rodriguez Hernandez, G.; Warner, J. H.; Briggs, G. A. D.; Mol, J. A.; Bhaskaran, H. Scaling Limits of Graphene Nanoelectrodes. *Nano Letters* **2017**, *17*, 3688–3693.
- (21) Lee, J. K.; Lee, G.-D.; Lee, S.; Yoon, E.; Anderson, H. L.; Briggs, G. A. D.; Warner, J. H. Atomic Scale Imaging of Reversible Ring Cyclization in Graphene Nanoconstrictions. *ACS Nano* **2019**, *13*, 2379–2388.
- (22) Pósa, L.; El Abbassi, M.; Makk, P.; Santa, B.; Nef, C.; Csontos, M.; Calame, M.; Halbritter, A. Multiple Physical Time Scales and Dead Time Rule in Few-Nanometers Sized Graphene–SiO<sub>x</sub>-Graphene Memristors. *Nano letters* **2017**, *17*, 6783–6789.
- (23) Murali, R.; Yang, Y.; Brenner, K.; Beck, T.; Meindl, J. D. Breakdown current density of graphene nanoribbons. *Applied Physics Letters* **2009**, *94*, 243114.
- (24) Hwang, E.; Adam, S.; Sarma, S. D. Carrier transport in two-dimensional graphene layers. *Physical review letters* **2007**, *98*, 186806.

- (25) Stauber, T.; Peres, N.; Guinea, F. Electronic transport in graphene: A semiclassical approach including midgap states. *Physical Review B* **2007**, *76*, 205423.
- (26) Sohler, T.; Calandra, M.; Park, C.-H.; Bonini, N.; Marzari, N.; Mauri, F. Phonon-limited resistivity of graphene by first-principles calculations: Electron-phonon interactions, strain-induced gauge field, and Boltzmann equation. *Physical Review B* **2014**, *90*, 125414.
- (27) Suzuura, H.; Ando, T. Electron lifetime due to optical-phonon scattering in a graphene sheet. *Journal of Physics: Conference Series*. 2009; p 022080.
- (28) Shishir, R.; Ferry, D. Velocity saturation in intrinsic graphene. *Journal of Physics: Condensed Matter* **2009**, *21*, 344201.
- (29) Song, J. C.; Reizer, M. Y.; Levitov, L. S. Disorder-assisted electron-phonon scattering and cooling pathways in graphene. *Physical review letters* **2012**, *109*, 106602.
- (30) Noshin, M.; Khan, A. I.; Navid, I. A.; Uddin, H. A.; Subrina, S. Impact of vacancies on the thermal conductivity of graphene nanoribbons: A molecular dynamics simulation study. *AIP Advances* **2017**, *7*, 015112.
- (31) Loh, G.; Teo, E. H. T.; Tay, B. K. Phonon localization around vacancies in graphene nanoribbons. *Diamond and related materials* **2012**, *23*, 88–92.
- (32) Liao, A.; Alizadegan, R.; Ong, Z.-Y.; Dutta, S.; Xiong, F.; Hsia, K. J.; Pop, E. Thermal dissipation and variability in electrical breakdown of carbon nanotube devices. *Physical Review B* **2010**, *82*, 205406.
- (33) Jiang, J.; Chu, J. H.; Banerjee, K. CMOS-compatible doped-multilayer-graphene interconnects for next-generation VLSI. 2018 IEEE International Electron Devices Meeting (IEDM). 2018; pp 34–5.

- (34) Tovee, P.; Pumarol, M.; Zeze, D.; Kjoller, K.; Kolosov, O. Nanoscale spatial resolution probes for scanning thermal microscopy of solid state materials. *Journal of Applied Physics* **2012**, *112*, 114317.

## Graphical TOC Entry

Some journals require a graphical entry for the Table of Contents. This should be laid out “print ready” so that the sizing of the text is correct.

Inside the tocentry environment, the font used is Helvetica 8 pt, as required by *Journal of the American Chemical Society*.

The surrounding frame is 9 cm by 3.5 cm, which is the maximum permitted for *Journal of the American Chemical Society* graphical table of content entries.

The box will not resize if the content is too big: instead it will overflow the edge of the box.

This box and the associated title will always be printed on a separate page at the end of the document.

Supplementary Information for  
Disorder enhanced electron-phonon scattering in graphene devices

**Charalambos Evangelis<sup>1,†,\*</sup>, Edward McCann<sup>3,†</sup>, Jacob L. Swett<sup>1</sup>, Sumit Tewari<sup>1</sup>,  
Xinya Bian<sup>1</sup>, James Thomas<sup>1</sup>, G. Andrew D. Briggs<sup>1</sup>, Oleg V. Kolosov<sup>3,\*</sup>, and  
Jan A. Mol<sup>2</sup>**

<sup>1</sup>Department of Materials, University of Oxford, Parks Road, OX1 3PH, Oxford, United Kingdom

<sup>2</sup>School of Physics and Astronomy, Queen Mary University of London, London E1 4NS, United Kingdom

<sup>3</sup>Department of Physics, Lancaster University, Bailrigg, LA1 4YB, Lancaster, United Kingdom

<sup>†</sup>Equal contribution

\*Corresponding author: [charalambos.evangelis@materials.ox.ac.uk](mailto:charalambos.evangelis@materials.ox.ac.uk), [o.kolosov@lancaster.ac.uk](mailto:o.kolosov@lancaster.ac.uk)

# 1. Scanning Thermal Microscopy

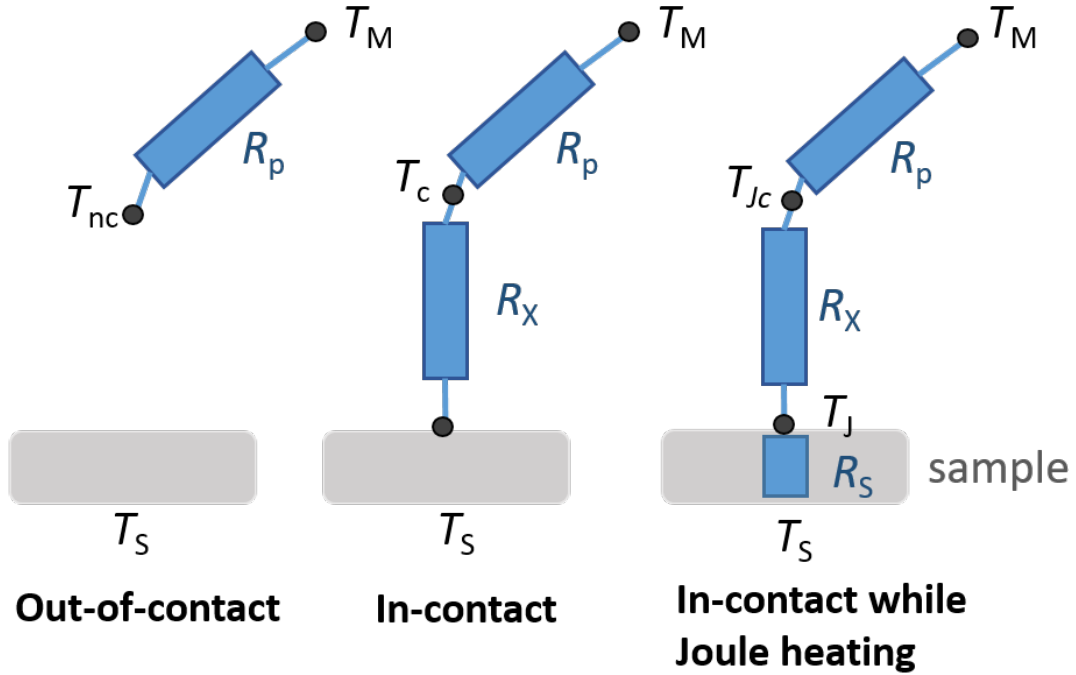
## 1.1 Temperature Measurement

When the SThM probe is brought in- and out- of contact to a non-biased graphene device the normalized temperature change between out- and in- contact is given by the formula: [1]

$$\frac{\Delta T_{nc} - \Delta T_c}{\Delta T_{nc}} = \frac{V_{nc} - V_c}{V_{nc}} = \frac{1}{R_p + R} \left( R_p + \frac{T_M - T_S}{Q_h} \right) \quad (1)$$

where  $T_M$  and  $T_S$  the macroscopic temperature of the microscope and the sample respectively which are being monitored by Pt-resistive elements,  $\Delta T_{nc} = T_{nc} - T_M$  and  $\Delta T_c = T_c - T_M$  are the excess temperatures of the probe when out- ( $T_{nc}$ ) and in- ( $T_c$ ) contact respectively, with respect to the microscope temperature,  $V_{nc}$  and  $V_c$  is the SThM signal for out- and in- contact respectively,  $R_p$  is the thermal resistance of the SThM probe,  $R_X$  is the thermal contact resistance of the tip-sample contact and  $Q_h$  is the heat generated in the probe heater. We maintain the temperature of the sample the same as the microscope ( $T_M = T_S$ ) by the use of a feedback controlled peltier stage and eq.1 takes the form:

$$\frac{\Delta T_{nc} - \Delta T_c}{\Delta T_{nc}} = \frac{V_{nc} - V_c}{V_{nc}} = \frac{R_p}{R_p + R} \quad (2)$$



Supplementary Figure 1: Thermal circuit of SThM tip and sample when the tip is out of contact, in-contact with the sample and in-contact with a Joule heated sample.

The heat generated in the probe heater when the tip is out-of-contact

$$Q_h = \frac{\Delta T_{nc}}{R_p}, \quad (3)$$

and in-contact with the graphene

$$Q_h = \frac{\Delta T_c}{R_p} + \frac{\Delta T_c}{R_X}. \quad (4)$$

By applying a voltage in the graphene device, the temperature of the graphene increases due to Joule heating, and correspondingly the heat generated in the probe becomes:

$$Q_h = \frac{\Delta T_j}{R_S} + \frac{\Delta T_{Jc} - \Delta T_j}{R_X} + \frac{\Delta T_{Jc}}{R_p}, \quad (5)$$

where  $\Delta T_{Jc} = T_{Jc} - T_M$  and  $\Delta T_j = T_j - T_S$  with  $T_{Jc}$  being the temperature measured on the probe resistor and  $T_j$  the temperature of the graphene-tip contact when graphene is Joule heated, and  $R_S$  is the whole sample including the macroscopic stage. Assuming a very high  $R_S$  the first term of eq.5 can be neglected and combining eq.2, eq.4 and eq.5 we can write

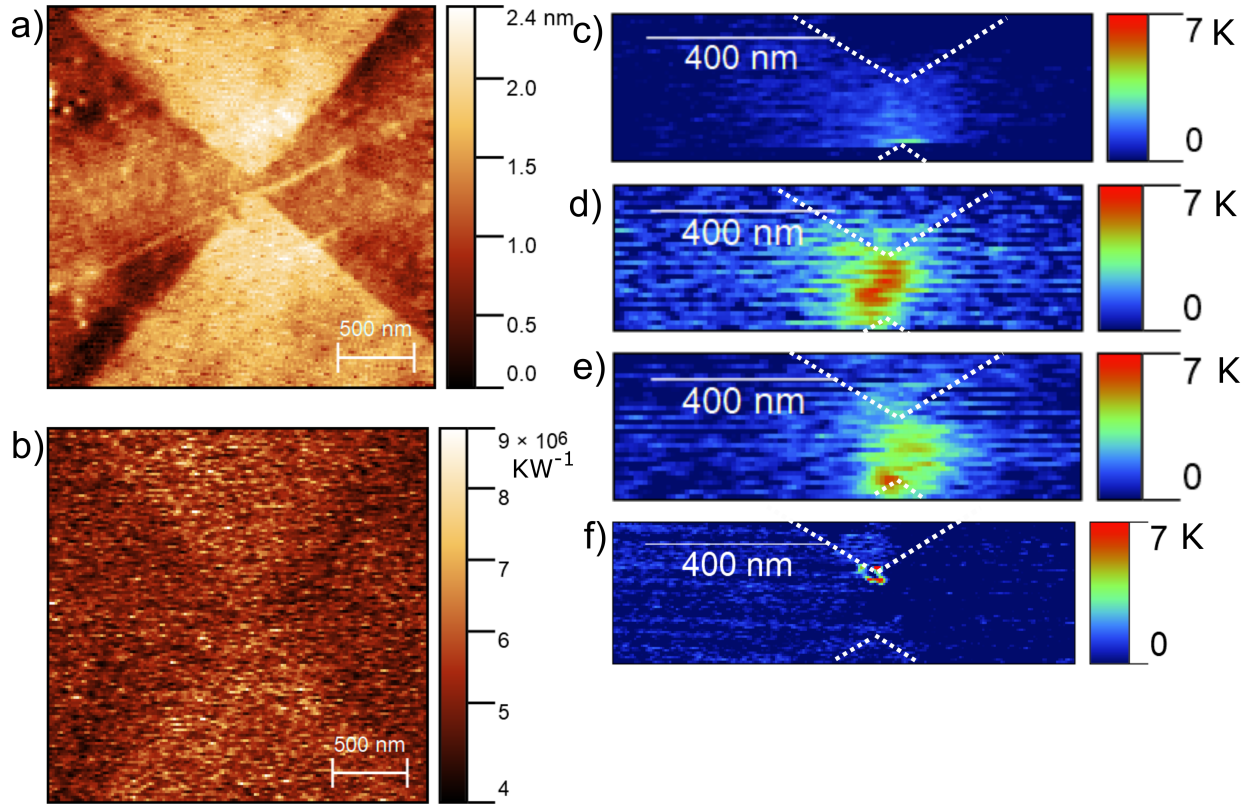
$$\Delta T_j = \frac{\Delta T_{nc}}{\Delta T_{nc} - \Delta T_c} (\Delta T_{Jc} - \Delta T_c), \quad (6)$$

where  $\frac{\Delta T_{nc}}{\Delta T_{nc} - \Delta T_c} = \frac{V_{nc}}{V_{nc} - V_c}$  is the inverse of the relative change of the SThM signal when the tip is in-contact with the non-heated graphene with respect to the out-of contact value and  $\Delta T_{Jc} - \Delta T_c$  is the excess temperature of the probe with respect to the initial tip-graphene temperature before Joule heating the graphene. The first part of eq.6 is obtained by recording approach-retraction cycles while no voltage is applied on the graphene device and the second is the excess temperature of the tip, as obtained from the SThM signal, while in-contact with the Joule heated graphene.

## 1.2 Tip effect on temperature measurement

The SThM tip can influence the measurement; and more specifically, the interfacial resistance between the SiO<sub>2</sub>-covered Si tip and the graphene, could further heat the graphene at the point of contact. The tip's lateral position and the contact area of tip-graphene are important. While the electrical resistance of the device increases, the lateral temperature distribution decreases (see fig.SI3 for the relevant temperature maps). This effect is much more important at high resistance values, which are not in the regime of validity of our model, where the Joule heating becomes very local. All the above make the absolute comparison of the temperature maps for different devices non-trivial. Although, as we keep the tip at the same lateral position during the experiment, the qualitative trend of the temperature with number of cycles is robust for each device.

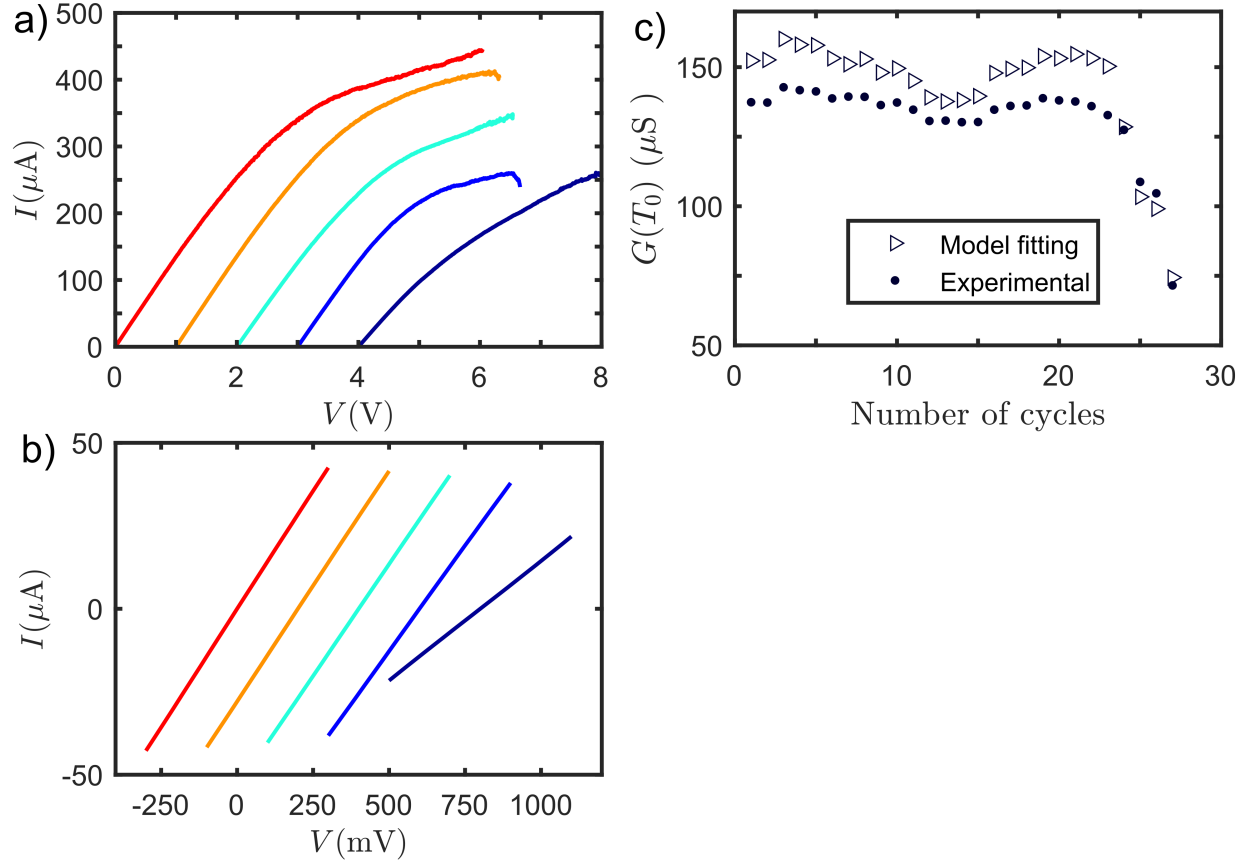
### 1.3 Thermal resistance and Temperature maps



Supplementary Figure 2: (a) Typical topography image of a bow-tie device. The SiO<sub>2</sub> at the topography image appears to be higher than the Graphene. This is possibly due to different friction between the two areas which causes a different torsion of the cantilever and therefore a cross-talk between the readout AFM photodetector channels. A second possible reason is some polymer residues remaining on the surface as a result of the lithography process. (b) Typical thermal resistance image acquired simultaneously with topography. Note that graphene is more thermally conductive (darker color) than SiO<sub>2</sub> (c,d,e,f) Temperature maps acquired at different steps of the controlled voltage ramp process. With white dotted line the edges of the graphene are shown. Note that  $P = 7, 210, 66, 23510 \mu\text{W}$  is applied at image c, d, e, f respectively

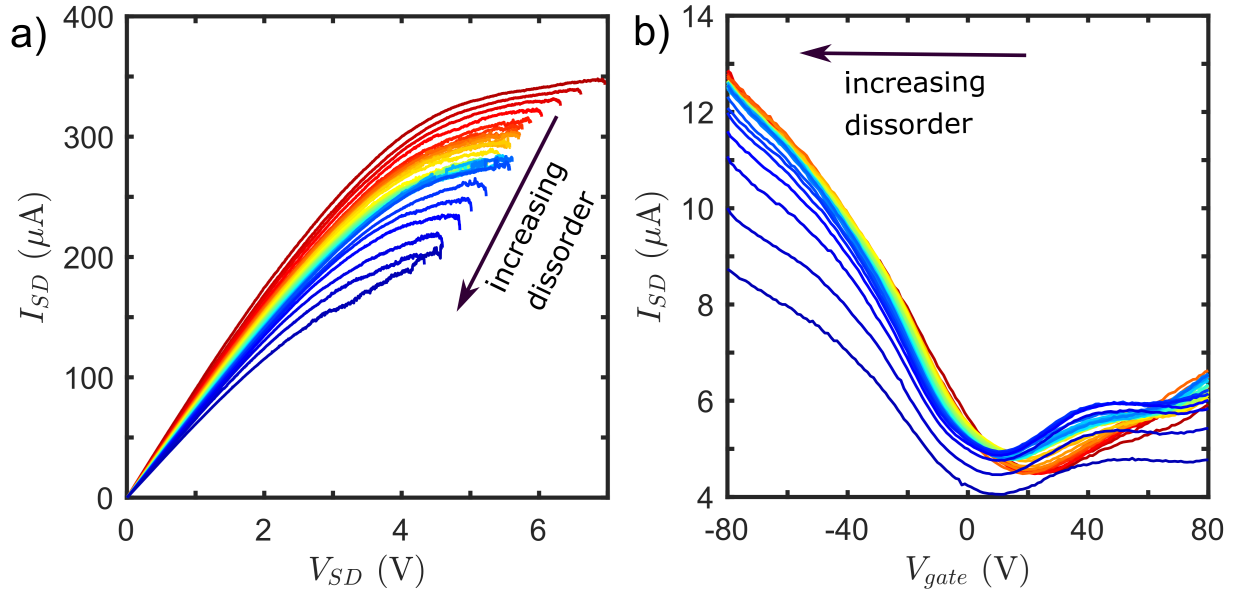
## 2. Electrical measurements

### 2.1. Electrical Resistance



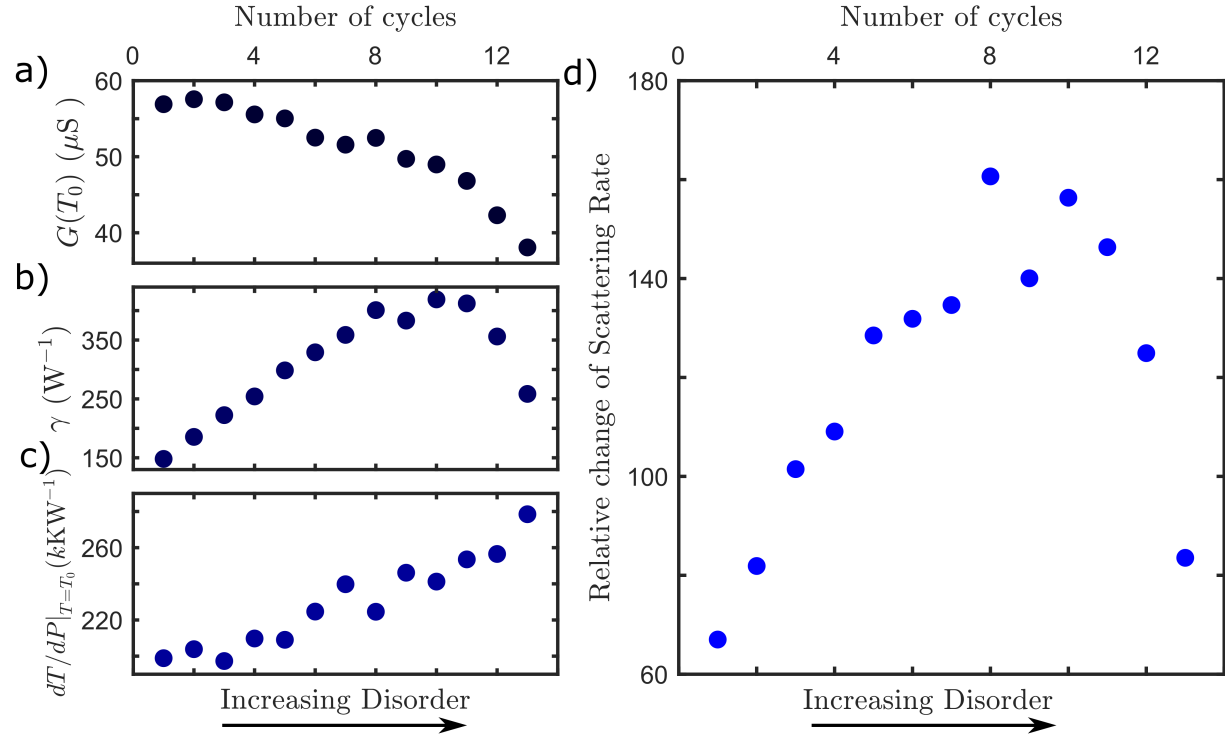
Supplementary Figure 3: (a,b) Examples of current versus voltage ramps during controlled breakdown process (a) and the corresponding small bias I-V curves recorded after each ramp for the electrical resistance estimation (b). (c) Resistance as measured after each voltage ramp (filled circles) and as calculated (open triangles) out fitting with the model.

## 2.2. Gate Traces



Supplementary Figure 4: (a,b) Current versus source-drain Voltage curves of the first cycles of feedback controlled breakdown of graphene devices (a) and the corresponding current versus gate voltage recorded after each source-drain voltage ramp (b). Note that, Dirac point minimum becomes less defined after each cycle (consistent with an increase in disorder) and the minimum shifts from positive gate voltages towards zero with the number of cycles, indicating a decrease of charge density.

### 3. Relative change of scattering rate of Device2



Supplementary Figure 5: (a,b,c,d) Conductance at room temperature  $G(T_0)$  (a), parameter  $\gamma$  (b),  $dT/dP|_{T=T_0}$  (c) and Relative change of Scattering rate (d) with the number of cycles (i.e. increasing disorder) for the device 2.  $G(T_0)$ ,  $\gamma$  and  $dT/dP|_{T=T_0}$  are extracted by fitting eq.6 and 2 of the main text to the I-V and P-T curves and then are used for the calculation of the relative change of  $\tau^{-1}$  with eq.4 of the main text.  $G(T_0)$ ,  $\gamma$ ,  $dT/dP|_{T=T_0}$  and relative change of Scattering rate of Device 2 has similar trends as Device 1 presented in the main text

## 4. Non-linear I(V) characteristics due to Joule heating and electron-phonon scattering.

We assume that the diffusive conductance  $G(T)$  has the usual Drude form wherein it is proportional to the momentum scattering time  $\tau(T)$  and all other parameters are temperature independent. With a Taylor expansion of  $\tau(T)$  around ambient temperature  $T_0$

$$\begin{aligned}\tau(T) &= \tau(T_0) \left[ 1 + \frac{(T - T_0)}{\tau(T_0)} \frac{d}{dT} \Big|_{T_0} + \dots \right] \\ &= \tau(T_0) \left[ 1 + (T - T_0) \frac{d \ln \tau}{dT} \Big|_{T_0} + \dots \right] \\ &= \tau(T_0) \left[ 1 - (T - T_0) \frac{d \ln \tau^{-1}}{dT} \Big|_{T_0} + \dots \right]\end{aligned}\tag{7}$$

the conductance may be written as

$$G(T) = G(T_0) \left[ 1 - (T - T_0) \frac{d \ln \tau^{-1}}{dT} \Big|_{T_0} + \dots \right]\tag{8}$$

Likewise, for the power dependence of the temperature  $T(P)$  perform a Taylor expansion around  $P = 0$

$$T - T_0 = P \frac{dT}{dP} \Big|_{T=T_0} + \dots\tag{9}$$

where  $T(0) = T_0$ . Substituting into the conductance:

$$G(T) = G(T_0) [1 - \gamma P + \dots]\tag{10}$$

where,

$$\gamma = \frac{dT}{dP} \Big|_{T=T_0} \frac{d \ln \tau^{-1}}{dT} \Big|_{T_0}\tag{11}$$

Then with  $P = IV$  and  $I = GV$ , we can express the current as

$$I = G(T_0) V - \gamma G(T_0) IV^2 + \dots\tag{12}$$

Now, substitute  $I = G(T_0) V$  into the second term:

$$I = G(T_0) V - \gamma G^2(T_0) V^3 + \dots\tag{13}$$

which is valid up to cubic order in  $V$ .

Alternatively, let's write the scattering rate  $\tau^{-1}(T) = \tau_d^{-1} + \tau_{ph}^{-1}(T)$  as a sum of a temperature-independent (disorder) part  $\tau_d^{-1}$  and a temperature-dependent (phonon) part  $\tau_{ph}^{-1}$ . Then the conductance may be expressed as

$$G(T) = G(T_0) \frac{\tau(T)}{\tau(T_0)} = \frac{G(T_0)}{\tau(T_0) [\tau_d^{-1} + \tau_{ph}^{-1}(T)]}\tag{14}$$

In particular, assume that the temperature dependent rate is linear in temperature  $\tau_{ph}^{-1}(T) \propto T$  so that

$$G(T) = \frac{G(T_0)}{\tau(T_0) \left[ \tau_d^{-1} + \tau_{ph}^{-1}(T_0) \left( \frac{T}{T_0} \right) \right]} \quad (15)$$

With this assumption  $\tau_{ph}^{-1}(T) \propto T$  and the definition of parameter  $\gamma$ , it is possible to write

$$\frac{T}{T_0} \approx 1 + \gamma P \tau^{-1}(T_0) \tau_{ph}(T_0) \quad (16)$$

so that the conductance simplifies as

$$G(T) \approx \frac{G(T_0)}{(1 + P)} \quad (17)$$

Then with  $P = IV$  and  $I = GV$ , we can express the current as

$$I \approx \frac{G(T_0) V}{(1 + IV)} \quad (18)$$

This is a quadratic equation for the current which can be solved as

$$I \approx \frac{1}{2\gamma V} (\sqrt{1 + 4\gamma G(T_0) V^2} - 1) \quad (19)$$

which is valid up to cubic order in  $V$  and agrees with  $I = G(T_0) V - \gamma G^2(T_0) V^3 + \dots$  up to that order.

## 5. Heat diffusion equation

To determine relevant parameters for heat transport, we consider the classical heat diffusion equation [2]

$$\kappa \frac{d^2 T(x)}{dx^2} + \frac{P}{A} - \frac{[T(x) - T_0]}{R_B} = 0 \quad (20)$$

where  $\kappa$  is the thermal conductivity. The second term accounts for Joule heating with power  $P$  in the graphene sample of area  $A$ , and the third term describes dissipation through the graphene-substrate interface with thermal boundary resistance  $R_B$ . Dividing by  $\kappa$  gives

$$\frac{d^2 T(x)}{dx^2} - \frac{[T(x) - T_0 - T_1]}{L_H^2} = 0 \quad (21)$$

where  $L_H = \sqrt{\kappa R_B}$  is the thermal healing length [3] and  $T_1 = PR_B/A$  is the characteristic increase in temperature due to Joule heating. Assuming that  $L_H$  is independent of temperature, and with boundary conditions  $T(x = -L/2) = T(x = L/2) = T_0$  for a system of length  $L$ , the solution is

$$T(x) = T_0 + T_1 \left[ 1 - \frac{\cosh(x/L_H)}{\cosh(L/2L_H)} \right] \quad (22)$$

Particularly, at the centre of the device  $T(x = 0) \approx T_0 + T_1$  for  $L \gg L_H$ . Alternatively, the mean temperature in the device

$$\langle T \rangle = \frac{1}{L} \int_{-L/2}^{L/2} T(x) dx = T_0 + T_1 \left[ 1 - \frac{2L_H}{L} \tanh(L/2L_H) \right] \quad (23)$$

also yields  $\langle T \rangle \approx T_0 + T_1$  for  $L \gg L_H$ . Thus, assuming  $L \gg L_H$ , near the constriction  $T \approx T_0 + T_1 = T_0 + PR_B/A$  yields  $T - T_0 \approx PR_B/A$ .

## 6. Electron momentum relaxation due to optical phonons

The electron-phonon scattering rate due to optical phonons with frequency  $\omega_{op}$  in graphene is given by [4–7]

$$\tau_{op}^{-1}(\epsilon) = \frac{D^2}{2\rho_m^2 v_F^2 \omega_{op}} \left[ g(\omega_{op}) |\epsilon + \omega_{op}| \frac{1 - f(\epsilon + \omega_{op})}{1 - f(\epsilon)} + (g(\omega_{op}) + 1) |\epsilon - \omega_{op}| \frac{1 - f(\epsilon - \omega_{op})}{1 - f(\epsilon)} \right] \quad (24)$$

where  $\epsilon = \pm v_F k$  is the electronic energy measured with respect to charge neutrality with Fermi velocity  $v_F$  and wave vector  $k$ ,  $f(\epsilon)$  is the Fermi-Dirac distribution and  $g(\omega)$  is the Bose-Einstein distribution. The two terms account for phonon absorption and emission, respectively, as  $|\epsilon + \omega_{op}|$  and  $|\epsilon - \omega_{op}|$  indicate the final electronic density of states, and this expression includes both inter- and intraband processes. In the prefactor,  $D$  is a deformation-potential coupling constant and  $\rho_m$  is the mass density of graphene. Given that  $\omega_{op} \approx 200$  meV in graphene, we expect this scattering rate to be negligible near room temperature and for electronic energy near the chemical potential  $\mu$ . In particular, taking into account the form of  $f(\epsilon)$  and  $g(\omega)$ , we simplify the absorption and emission terms for  $k_B T \ll \omega_{op}$  as

$$\frac{1}{\tau^{op}(\epsilon)} = \frac{D_\eta^2}{2\rho_m \omega_\eta \hbar^2 v_F^2} \left[ g(\omega_\eta) |\epsilon + \hbar\omega_\eta| \left( \frac{1 - f^0(\epsilon + \hbar\omega_\eta)}{1 - f^0(\epsilon)} \right) + (g(\omega_\eta) + 1) |\epsilon - \hbar\omega_\eta| \left( \frac{1 - f^0(\epsilon - \hbar\omega_\eta)}{1 - f^0(\epsilon)} \right) \right], \quad (25)$$

$$\left(\frac{1}{\tau^{\text{op}}(\epsilon)}\right)_{ab} \approx C \begin{cases} \frac{|\epsilon + \hbar\omega_\eta|}{\hbar\omega_\eta} & \text{for } \epsilon < \mu - \hbar\omega_\eta \\ \frac{|\epsilon + \hbar\omega_\eta|}{\hbar\omega_\eta} e^{-(\epsilon + \hbar\omega_\eta - \mu)/k_B T} & \text{for } \mu - \hbar\omega_\eta < \epsilon < \mu \\ \frac{|\epsilon + \hbar\omega_\eta|}{\hbar\omega_\eta} e^{-\hbar\omega_\eta/k_B T} \approx 0 & \text{for } \epsilon > \mu \end{cases} \quad (26)$$

$$\left(\frac{1}{\tau^{\text{op}}(\epsilon)}\right)_{em} \approx C \begin{cases} \frac{|\epsilon - \hbar\omega_\eta|}{\hbar\omega_\eta} e^{-\hbar\omega_\eta/k_B T} \approx 0 & \text{for } \epsilon < \mu \\ \frac{|\epsilon - \hbar\omega_\eta|}{\hbar\omega_\eta} e^{-(\mu + \hbar\omega_\eta - \epsilon)/k_B T} & \text{for } \mu < \epsilon < \mu + \hbar\omega_\eta \\ \frac{|\epsilon - \hbar\omega_\eta|}{\hbar\omega_\eta} & \text{for } \epsilon > \mu + \hbar\omega_\eta \end{cases} \quad (27)$$

which are only significant for electronic energy  $\sim \omega_{op}$  away from the chemical potential, e.g. the final line describes a process whereby an electron initially in a high-energy state with  $\epsilon > \mu + \omega_{op}$  emits a phonon and ends in a final state near the chemical potential with density of states  $\propto |\epsilon - \omega_{op}| \sim |\mu|$ .

## References

1. Evangeli, C. *et al.* Nanoscale Thermal Transport in 2D Nanostructures from Cryogenic to Room Temperature. *Advanced Electronic Materials* (2019).
2. Dorgan, V. E., Behnam, A., Conley, H. J., Bolotin, K. I. & Pop, E. High-field electrical and thermal transport in suspended graphene. *Nano letters* **13**, 4581–4586 (2013).
3. Liao, A. *et al.* Thermal dissipation and variability in electrical breakdown of carbon nanotube devices. *Physical Review B* **82**, 205406 (2010).
4. Suzuura, H. & Ando, T. Zone-boundary phonon in graphene and nanotube. *Journal of the Physical Society of Japan* **77**, 044703–044703 (2008).
5. Suzuura, H. & Ando, T. *Electron lifetime due to optical-phonon scattering in a graphene sheet* in *Journal of Physics: Conference Series* **150** (2009), 022080.
6. Shishir, R. & Ferry, D. Intrinsic mobility in graphene. *Journal of Physics: Condensed Matter* **21**, 232204 (2009).
7. Sohler, T. *et al.* Phonon-limited resistivity of graphene by first-principles calculations: Electron-phonon interactions, strain-induced gauge field, and Boltzmann equation. *Physical Review B* **90**, 125414 (2014).